J. Fluid Mech. (1998), *vol.* 374, *pp.* 379–405. Printed in the United Kingdom

Direct numerical simulation of a separated turbulent boundary layer†

By Y. NA AND P. MOIN‡

Department of Mechanical Engineering, Stanford University, Stanford, CA 94305, USA

(Received 25 July 1997 and in revised form 22 January 1998)

A separated turbulent boundary layer over a flat plate was investigated by direct numerical simulation of the incompressible Navier–Stokes equations. A suction-blowing velocity distribution was prescribed along the upper boundary of the computational domain to create an adverse-to-favourable pressure gradient that produces a closed separation bubble. The Reynolds number based on inlet free-stream velocity and momentum thickness is 300. Neither instantaneous detachment nor reattachment points are fixed in space but fluctuate significantly. The mean detachment and reattachment locations determined by three different definitions, i.e. (i) location of 50% forward flow fraction, (ii) mean dividing streamline ($\psi = 0$), (iii) location of zero wall-shear stress ($\overline{\tau}_w = 0$), are in good agreement. Instantaneous vorticity contours show that the turbulent structures emanating upstream of separation move upwards into the shear layer in the detachment region and then turn around the bubble. The locations of the maximum turbulence intensities as well as Reynolds shear stress occur in the middle of the shear layer. In the detached flow region, Reynolds shear stresses and their gradients are large away from the wall and thus the largest pressure fluctuations are in the middle of the shear layer. Iso-surfaces of negative pressure fluctuations which correspond to the core region of the vortices show that large-scale structures grow in the shear layer and agglomerate. They then impinge on the wall and subsequently convect downstream. The characteristic Strouhal number $St = f\delta^*_{in}/U_0$ associated with this motion ranges from 0.0025 to 0.01. The kinetic energy budget in the detachment region is very similar to that of a plane mixing layer.

1. Introduction

Understanding the onset of separation and subsequent reattachment of turbulent flows has considerable practical significance because they are related to the upper limit of efficiency for many aerodynamic devices such as diffusers, turbine blades, lifting bodies etc. In spite of the many experimental studies on separated flows, the structure of the separated region is not fully understood. The reason, as pointed out by Simpson, Chew & Shivaprasad (1981*a*, *b*), is partly due to the lack of proper instrumentation in early studies. Even with the advent of pulsed wire and directionally sensitive laser anemometers, the velocity measurements in the separated zone are still subject to errors caused by velocity bias (Adams & Eaton 1988). Simpson (1985) reviewed in much detail the early experimental and computational works which were followed by updated reviews in Simpson (1989, 1991).

† This article first appeared in volume 370, pp. 175–201 without p. 200. This reprinting replaces that version and it will be the one that is referenced.

‡ Also with NASA Ames Research Center.

In many turbulent separated flows (e.g. flow around turbine blades, airfoils), both the surface curvature and adverse pressure gradient (APG hereinafter) influence the detachment and subsequent evolution of turbulent boundary layers. To isolate the effects of the APG it would be instructive to consider a flat plate surface with an imposed APG. Although there are many studies of flows with a *closed* separation bubble, most of the test geometries involved sharp edges (e.g. backward facing step, fence) or rapidly varying surface curvature producing fixed separation points. Currently, only a limited number of measurements of separated flows on a flat plate are available.

Simpson, Strickland & Barr's (1977) pioneering work on separating turbulent boundary layers with an airfoil-type pressure distribution revealed several important features of these flows. They showed that the law-of-the-wall velocity profile scaling is valid up to intermittent separation, and normal stress terms in the momentum and the kinetic energy equations are important near separation. Later studies by Simpson *et al.* (1981*a*, *b*) and Shiloh, Shivaprasad & Simpson (1981) demonstrated that the backflow velocity profiles are not consistent with the law-of-the-wall type scaling and the turbulent velocity fluctuations within the backflow are comparable to the mean flow velocities.

Perry & Fairlie (1975) studied a suddenly separating and reattaching turbulent boundary layer on a flat surface. Their inviscid model, which assumes that the separation process is dominated by the interaction between the vortical region and the irrotational field outside the separation bubble, has been shown to be capable of predicting the gross properties of their experiment.

In Cutler & Johnston's (1984) experiment, complete detachment of the boundary layer was not achieved but they drew some significant conclusions as follow: (i) Since the mean streamline angle to the wall is not small near the separation region even though the wall is flat it becomes important to model the turbulent shear stress in coordinates locally orthogonal to the streamlines. (ii) The effect of the mean streamline curvature is to reduce the shear stress and the entrainment of the free-stream fluid into the boundary layer.

Patrick (1987) performed an experimental study of a very large-scale closed separation bubble on a flat plate test surface. He corroborated Simpson *et al.*'s (1981*a*, *b*) findings and showed that the reattachment zone is highly unsteady and characterized by low-frequency streamline flapping with large-scale eddies being convected alternately up- and downstream from the impingement point on the test surface.

Like experiments, only a limited number of numerical works on separated flows over a flat plate are available. Because of limitations of current turbulence models (Kline, Cantwell & Lilley 1982), many prediction methods based on the Reynolds-averaged equations are not reliable in separated flows. Comprehensive databases, especially Reynolds stress equation budgets, would be valuable for progress in this area. Briley & McDonald (1975) performed computations of thin incompressible separation bubbles on smooth surfaces by solving the steady boundary layer and Navier–Stokes equations for the flow in the immediate vicinity of the bubble. A viscous–inviscid interaction model which accounts for the elliptic interaction between the shear layer and inviscid free stream was employed, and computed solutions for transitional separation bubbles on an airfoil were in reasonable agreement with the available data.

Recently Coleman & Spalart (1993) performed a direct numerical simulation (DNS hereinafter) of a very weakly separated turbulent boundary layer. To account for the streamwise flow inhomogeneity while allowing the use of the Fourier series in the

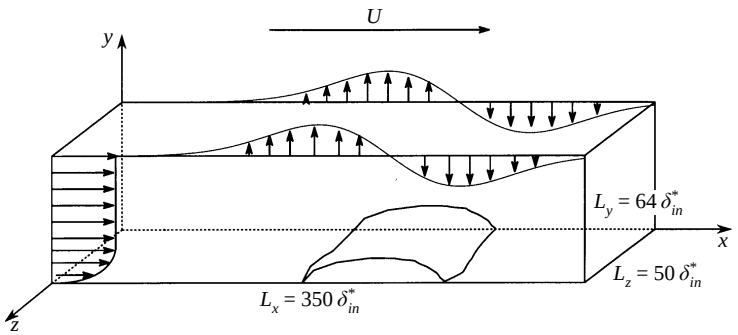

FIGURE 1. Computational domain of separated turbulent boundary layer.

streamwise direction, they modified the Navier–Stokes equations so that in the regions where the equations are not valid, at the upstream and downstream regions of the computational domain, the outflowing turbulence is converted into an appropriate inflow. The strong APG was found to lead to the disappearance of the near-wall streaks that are observed in weak or favourable pressure gradient (FPG hereinafter) flows and the zero skin friction point closely corresponds to the 50% flow-reversal locations.

The present direct numerical simulation is the most extensive and detailed computation of a spatially evolving separated turbulent boundary layer over a flat plate with inflow/outflow boundary conditions performed to date. This paper attempts to provide physical insight into the characteristics of this flow and a comprehensive database containing complete budgets of the Reynolds stresses for improving turbulent models.

2. Numerical methodology

2.1. *Computational domain*

The schematic diagram of three-dimensional computational domain is shown in figure 1. The streamwise extent of the domain is $L_x = 350\delta^*_{in}$, the vertical height is $L_y = 64\delta^*_{in}$ and the spanwise extent is $L_z = 50\delta^*_{in}$, where δ^*_{in} is the inlet displacement thickness. The origin of the coordinate system used is located at the lower corner as indicated in figure 1.

The Reynolds number based on inlet momentum thickness and maximum mean streamwise velocity at the inlet, Re_θ, is 300. Inflow turbulence was generated using the method described in § 2.3 and the mean velocity profile at the inlet needed for specifying the inflow boundary condition was obtained from Spalart's (1988) zero pressure gradient (ZPG hereinafter) boundary layer simulation at the same Reynolds number.

The time-dependent Navier–Stokes and continuity equations for incompressible flow with constant kinematic viscosity are

$$\frac{\partial}{\partial t}u_i + \frac{\partial}{\partial x_k}u_i u_k = -\frac{\partial}{\partial x_i}p + \frac{1}{Re_{\delta^*_{in}}}\frac{\partial^2}{\partial x_k \partial x_k}u_i, \tag{1}$$

$$\frac{\partial}{\partial x_k}u_k = 0. \tag{2}$$

All variables are non-dimensionalized by the maximum mean velocity at the inlet, U_0, and the inlet displacement thickness, δ^*_{in}. The subscripts i, j, k take values of 1, 2, 3 to denote the streamwise (x), wall-normal (y) and spanwise (z) directions, respectively. The u_i are the velocity components and p the static pressure. The Reynolds number $Re_{\delta^*_{in}}$ is defined by the displacement thickness at the inlet, δ^*_{in}, and maximum mean inlet velocity, U_0.

The governing equations (1) and (2) are integrated in time using a semi-implicit scheme. A low-storage three-substep, third-order Runge–Kutta scheme (Spalart, Moser & Rogers 1991) is used for treating convective terms explicitly and a second-order Crank–Nicolson scheme is used for treating viscous terms implicitly. The three-substep Runge–Kutta scheme is combined with the modified fractional step procedure (Le & Moin 1991). Le & Moin's method allows the velocity field to be advanced through the substeps without satisfying the continuity equation at each Runge–Kutta substep. The divergence-free velocity field is obtained only at the last substep by solving the Poisson equation for pressure. The resulting algorithm is described in detail in Le, Moin & Kim (1997).

The governing equations are solved on a rectangular staggered grid (Harlow & Welch 1965). The pressure is defined at the centre of the cell and velocity components on the faces. All spatial derivatives are approximated with second-order central difference schemes. Grid spacings are uniform in both streamwise and spanwise directions. This uniform mesh allows the use of transform methods in the solution of Poisson equation for pressure. The geometry of the present separated flow contains several regions of non-negligible gradients which require careful resolution. Grid clustering is required in the wall-normal direction very near the wall to resolve the boundary layer. Applying suction and blowing through the upper boundary creates non-negligible gradients in both streamwise and normal directions. Thus, the grid stretching with increased spacing in the wall-normal direction near the upper boundary as in a ZPG turbulent boundary layer is not desirable. In the present study, nearly uniform grid spacing was maintained near the upper boundary and two hyperbolic tangent functions with different parameters were used for grid stretching. A total of 513 computational cells are used in the streamwise direction, 193 cells in the wall-normal direction and 129 cells in the spanwise direction. Based on the inlet wall shear velocity, u_τ, the grid spacing in the streamwise direction is $\Delta x^+ \approx 18.3$ in wall units. In the wall-normal direction, the minimum grid spacing is $\Delta y^+_{min} \approx 0.11$ at the wall and the maximum grid spacing is $\Delta y^+_{max} \approx 22.7$ in the free stream. In the spanwise direction, grid spacing is $\Delta z^+ \approx 10.5$ in wall units.

Extensive grid-independence studies were performed to ensure adequacy of the above grid spacings. These studies show the following. (*a*) The streamwise resolution of at least 513 cells is required and the higher resolution in this direction does not make significant changes to the first-order statistics (e.g. skin-friction and wall-pressure coefficients C_f, C_p) and mean velocity profiles. (*b*) The resolution in the wall-normal direction can make significant changes to C_f if less than 161 cells are used. However, higher resolution did not improve the first-order statistics. (*c*) As the resolution in the streamwise and wall-normal direction gets better, the C_f in the recovery region decreases. Figure 2 shows the comparison of mean velocity profiles at several streamwise locations. The velocity profiles with ($769 \times 161 \times 129$), ($513 \times 193 \times 129$) and ($513 \times 225 \times 129$) grids are in good agreement throughout the domain. In the middle of the separation bubble ($x/\delta^*_{in} = 220$), the height of the mean backflow region is approximately the same for all three computational resolutions considered.

One-dimensional spanwise energy spectra at several streamwise locations show

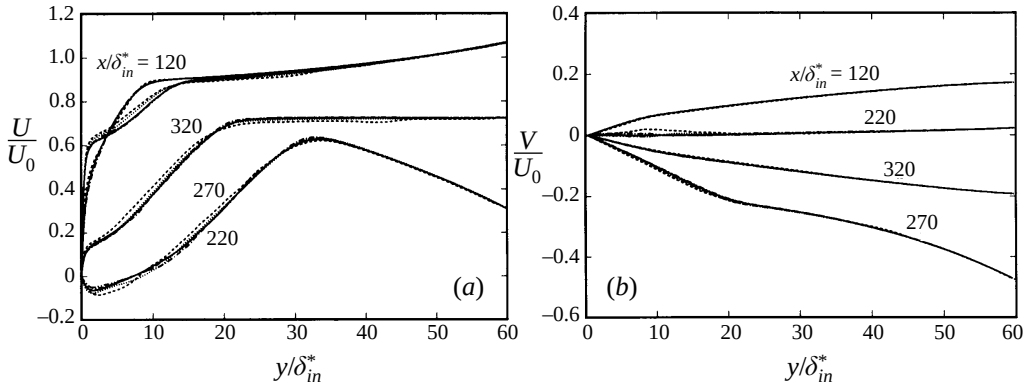

FIGURE 2. Comparison of mean velocity. (*a*) Streamwise velocity; (*b*) wall-normal velocity: – – – –, $513 \times 129 \times 129$; ·····, $513 \times 161 \times 129$; —·—, $769 \times 161 \times 129$; ———, $513 \times 193 \times 129$; —··—, $513 \times 225 \times 129$.

sufficient energy drop at high wavenumbers (Na & Moin 1996) indicating that the resolution in the spanwise direction is adequate.

2.2. *Boundary conditions*

The no-slip boundary condition is used along the lower boundary of the computational domain. The flow is assumed to be homogeneous in the spanwise direction, justifying the use of periodic boundary conditions in that direction.

Specification of velocity boundary conditions in the free stream is not trivial because it is, in general, not known *a priori* which boundary conditions would lead to a specified pressure gradient. In many experiments, velocities are measured from the wall only up to the region just outside the boundary layer and since the upper boundary of the computational domain is usually located far away from the boundary layer, it is not possible to get the velocity information along the upper boundary directly from the experiment.

One way of obtaining approximate but reasonable boundary conditions is to use a potential flow solution (from the panel method, for example). Several iterations of viscous–inviscid calculations are unavoidable for improving the solution. Given the streamwise velocity at the edge of boundary layer, one can compute the corresponding wall-normal velocity at the same location as well as the streamwise and wall-normal velocity distributions $U_{top}(x)$ and $V_{top}(x)$ along the upper boundary of the computational domain. Our work on the free-stream boundary conditions in the ZPG and the APG turbulent boundary layer flows without separation revealed that numerical oscillations are obtained away from the wall when both the streamwise velocity $U_{top}(x)$ and the normal velocity $V_{top}(x)$ are simultaneously prescribed. A physically realistic boundary condition is to prescribe $V_{top}(x)$ and to let the streamwise velocity adjust itself by imposing a zero-vorticity condition. The wall-normal velocity, $V_{top}(x)$ and the normal derivative of the streamwise velocity are then prescribed as the well-posed boundary conditions for Navier–Stokes computations:

$$\left.\begin{aligned} v(x, L_y, z, t) &= V_{top}(x), \\ \left.\frac{\partial u}{\partial y}\right|_{x,L_y,z,t} &= \frac{\mathrm{d}V_{top}(x)}{\mathrm{d}x}, \quad \left.\frac{\partial w}{\mathrm{d}y}\right|_{x,L_y,z,t} = 0. \end{aligned}\right\} \tag{3}$$

Figure 3 shows the prescribed suction–blowing distribution of $V_{top}(x)$ which leads

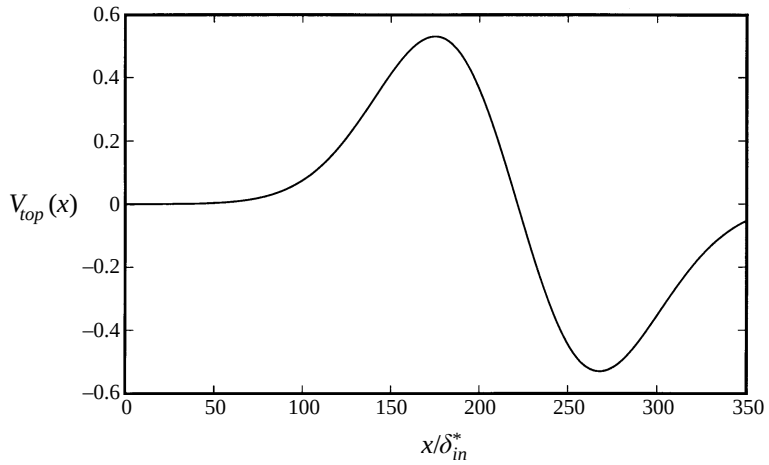

FIGURE 3. Suction–blowing velocity distribution along the upper boundary.

to the APG needed to produce a separation bubble. The strong FPG induced by the blowing portion of the velocity distribution causes the layer to firmly reattach after the flow separates. The maximum $V_{top}(x)$ was adjusted so that the height of the separation bubble is about two inlet boundary layer thicknesses. To help the flow develop from the initial transient associated with the inflow boundary condition, $V_{top}(x)$ was adjusted so that the flow evolves under a mildly FPG near the inlet of the computational domain. The upper boundary is located far enough from the vortical region to ensure the validity of the zero-vorticity condition (3). The numerical solution with this boundary condition did not exhibit any numerical problems in the free stream.

An exit boundary condition is needed that performs well for both boundary layers and propagating structures. This boundary condition must allow the turbulence structures generated inside the domain to smoothly leave the computational domain. The convective boundary condition

$$\frac{\partial u_i}{\partial t} + U_c \frac{\partial u_i}{\partial x} = 0, \tag{4}$$

where U_c is the convection velocity at the exit, was used by Lowery & Reynolds (1986) and later by Pauley, Moin & Reynolds (1990), Le *et al.* (1997) and many others. Pauley *et al.* showed that the inclusion of one or more viscous terms in (4) leads to numerical instability. The convection velocity U_c is set equal to the mean streamwise velocity integrated across the exit plane, which was demonstrated to work well in a turbulent flow by Le *et al.* (1997). Equation (4) is integrated in time using the explicit Euler approximation. Examination of statistical quantities from the present simulations indicates that the effects of the exit boundary condition is confined within one inlet boundary layer thicknesses from the exit.

2.3. *Method of generating inflow turbulence*

A good strategy for prescription of the unsteady, stochastic inflow conditions would lead to a significant reduction in the computational cost. The approach of Lee, Lele & Moin (1992) and Le *et al.* (1997) was to prescribe velocity fluctuations superimposed on a mean profile with a specified power spectrum and random phase. However, the resulting inflow turbulence lacked structural features and required relatively long

spatial development for the flow to become physically realistic. Le *et al.* found that for their DNS calculation of backward-facing step flow approximately 10 step heights (one step height is approximately equal to 1.2 boundary layer thickness) were required for the flow to recover before reaching the step.

Our present technique consists of a sequential feeding at the inflow plane of a frozen DNS field with randomization of amplitude factors (Mahesh, Moin & Lele 1996). Phase angle information is considered more important than the amplitude factor in that it is closely related to turbulence structures. Thus, to minimize the alteration of the structures of a DNS field, the corresponding phase angles are kept unchanged during the process of generating inflow turbulence. In this manner, physically realistic velocity fluctuations, using an already validated DNS field are generated and then superposed on a mean velocity profile at the inflow plane. The mean velocity profile is taken from Spalart's (1988) temporal simulation of ZPG turbulent boundary layer at Reynolds number 300 based on momentum thickness. Using a single realization of Spalart's instantaneous three-dimensional flow field, velocity fluctuations $u'_j(x, y, z)$, $j = 1, 2, 3$, at an instant can be calculated by subtracting the mean velocity $\overline{u}_j(y)$ from the instantaneous velocity $u_j(x, y, z)$,

$$u'_j(x, y, z) = u_j(x, y, z) - \overline{u}_j(y), \tag{5}$$

where overbar denotes the average over the streamwise and spanwise directions and time. By taking the Fourier transform of u'_j in the streamwise and spanwise directions, the Fourier coefficient $\hat{u}'_j(k_x, y, k_z)$ at a given y can be obtained:

$$\hat{u}'_j = |\hat{u}'_j| \mathrm{e}^{\mathrm{i}\phi}. \tag{6}$$

In the Fourier space, a new field of $(\hat{u}'_j)_{new}$ is formed by jittering $\hat{u}'_j$ by random numbers α_u:

$$\begin{aligned} (\hat{u}'_j)_{new} &= \alpha_u(k_x, y, k_z)\hat{u}'_j \\ &= |(\hat{u}'_j)_{new}| \mathrm{e}^{\mathrm{i}\phi} \end{aligned} \tag{7}$$

where α_u is a real number in the range $0.8 \leqslant \alpha_u \leqslant 1.2$. Then, the signal $(u'_j)_{new}$ in the physical space as a function of x, y and z is obtained through the inverse Fourier transform of $(\hat{u}'_j)_{new}$. The purpose of introducing random number α_u in (7) is to recycle a DNS field with minimal periodicity effect. This newly generated signal is superimposed on a mean profile and fed into the computational domain using Taylor's hypothesis. In other words, the streamwise coordinate x is converted to time t using the relation

$$x = U_c t, \tag{8}$$

where U_c is the convection velocity. The simulations with different values of U_c ($= 0.8U_0$ and $1.0U_0$) made negligible difference in the statistical results for the case of ZPG turbulent boundary layer flows. Thus, $U_c = 1.0U_0$ was chosen and the fluctuation signals were generated to conform to the corresponding prescribed turbulence intensities $\overline{u'^2_j}$ of Spalart's simulation.

After feeding all the planes of the newly generated field, another set of planes is generated using (7) with a new set of α_u by recycling the original flow field given in (6). One might be concerned about the effect of the recycling time scale or period, T_{sp}, imposed on the solutions of the present study. The periodicity can be significantly reduced by increasing the range of the random number, α_u, in (7). However, in the present study, α_u was chosen to be in the range $0.8 \leqslant \alpha_u \leqslant 1.2$ to retain the structure

of Spalart's DNS field as much as possible. Even though the turbulent signal at the inlet is nearly periodic, the time histories of wall pressure at various stations in the separated flow do not exhibit characteristics associated with the 'period' of the inflow signal, and the space–time correlations of wall-pressure fluctuations shown in Na & Moin (1996) also indicate that the effect of the inlet quasi-periodicity is negligible.

DNS of a ZPG turbulent boundary layer and the APG boundary layer of Watmuff's (1989) experiment with this inflow turbulence shows that the flow recovers very quickly after the short transition length. The evolution of C_f indicates that about $3\delta_{in}$ is required for the recovery. More details are discussed in Na & Moin (1996). The numerical code is validated by the good agreement between the DNS solution and Watmuff's experimental data.

2.4. *Calculation of statistical quantities*

Statistical averages were performed over the homogeneous spanwise direction and time and hence single-point statistics are functions of both x and y. In the present simulation, the flow separates due to the large APG induced by the suction–blowing velocity distribution $V_{top}(x)$ and neither instantaneous detachment nor reattachment points are fixed in space but fluctuate significantly. This unsteady, complex flapping motion causes very slow statistical convergence in the separated and subsequent reattachment zones, most likely because of slow speeds or large time scales of eddies in the separation zone. Le *et al.* (1997) observed similar problems in their numerical study of the backward-facing step flow. Figure 4 shows the longitudinal Reynolds stress $\overline{u'u'}$ budgets at two streamwise locations, $x/\delta^*_{in} = 220$ and 320: $x/\delta^*_{in} = 220$ is located in the middle of the separation bubble and $x/\delta^*_{in} = 320$ is far downstream. Even though large-scale fluctuations exist at $x/\delta^*_{in} = 220$, a good balance was achieved. At this streamwise location where such fluctuations are larger than at any other location, maximum imbalance of 0.000 54, which is about 5% of the maximum production (at $y/\delta^*_{in} = 20.8$), occurs at $y/\delta^*_{in} = 23.8$. Far downstream of the separation bubble, Reynolds stress budgets are sufficiently smooth. As more samples are added, the profiles become smoother, although slowly, but the overall shapes of the terms hardly change. Thus, it was decided not to continue the simulation beyond this point in the interest of saving computer resources. A piecewise least-square fitting method using the Savitzky–Golay filter (Press *et al.* 1992) which was used in Le *et al.* (1997) was applied to the budgets presented in this paper for turbulence modelling applications. This fitting was applied to the budgets in the detachment and reattachment regions as well as inside the separation bubble. Fitting was not applied to the first- and second-order statistics. The statistical data were sampled at equal time intervals, $\Delta t_s = 0.3\delta^*_{in}/U_0$, or every 10 calculation time steps and the total averaging time was $T_{ave} = 2250\delta^*_{in}/U_0$. This is equivalent to about 7 flow-through times. The 'flow-through' time here is defined as the full trip time of fluid particles outside the separation bubble through the domain.

3. Results and discussion

3.1. *Instantaneous shape of the separation bubble*

Instantaneous velocity vectors in the (x, y)-plane at the middle of the spanwise domain at two different instants are presented in figure 5. The shape of the instantaneous separation bubble is clearly changing with time. The detachment and reattachment regions move significantly upstream and downstream indicating the highly unsteady

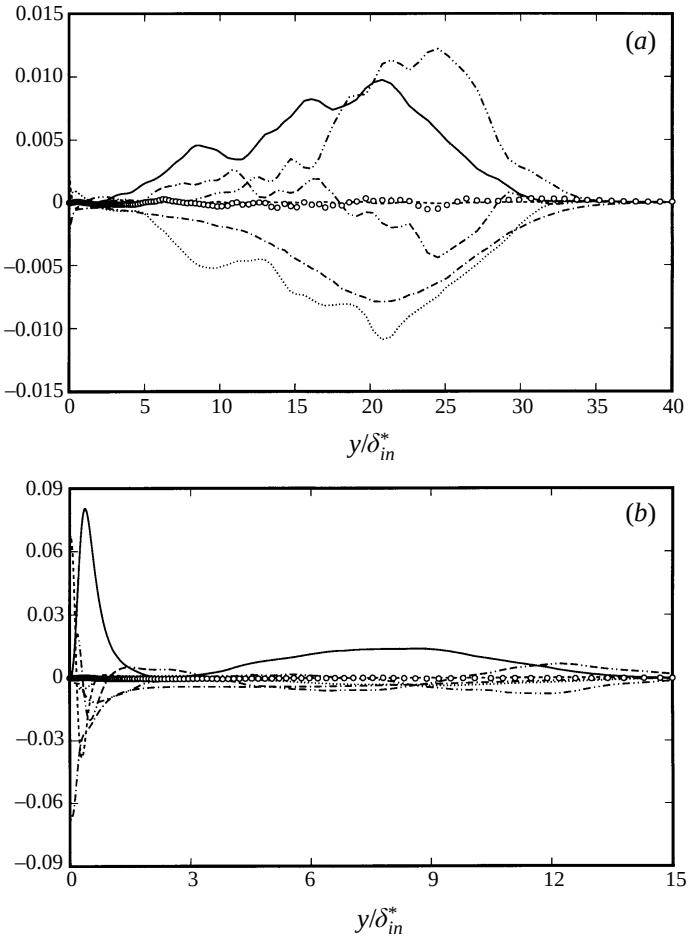

FIGURE 4. Longitudinal Reynolds-stress budget normalized by U_0^3/δ^*_{in} ($\times 10^2$). (*a*) $x/\delta^*_{in} = 220$; (*b*) $x/\delta^*_{in} = 320$: ———, production; —·—, dissipation; – – – –, viscous diffusion; —··—, convection; ——··, turbulent transport; ·····, velocity pressure gradient; ○, balance of terms.

nature of the flow in the separated zone even though the Reynolds number is relatively low.

3.2. *Instantaneous skin friction coefficient*

Figure 6 shows contours of the instantaneous skin friction coefficient (C_f) at two different instants. Solid and dotted lines denote positive and negative C_f, respectively. As the turbulent boundary layer experiences an APG, the flow near the wall decelerates until an intermittent backflow takes place and then massive reversed flow occurs. Some fluid elements with high momentum penetrate into the separated zone and others move upstream for a distance and then are carried downstream inside the bubble. These developments make the detachment zone highly three-dimensional. The coherent streaky structures which can be seen in the ZPG and FPG boundary layers are observed far upstream of the detachment region, but they disappear in the separated zone and then re-appear downstream of the reattachment region. It appears that the average spanwise spacing, λ_z, of the near-wall streaks, which is a function of the pressure gradient parameter, increases significantly in the recovery region.

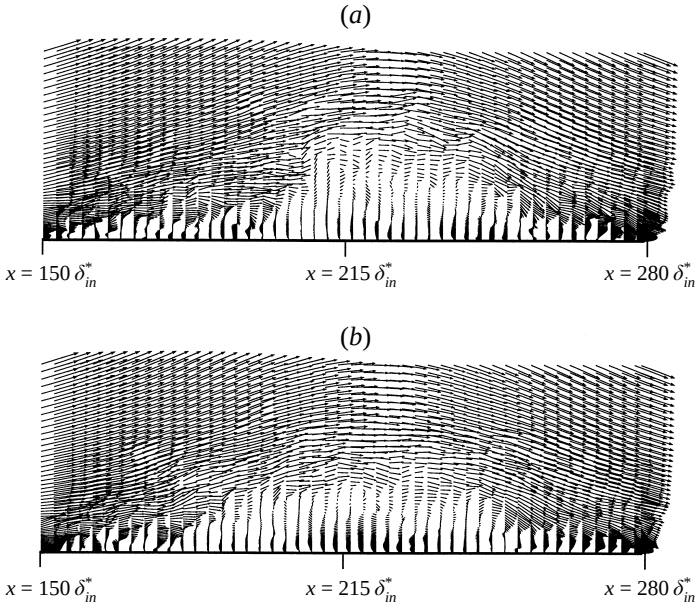

FIGURE 5. Instantaneous velocity vectors at $z/\delta^*_{in} = 25$ in the (x, y)-plane. (*a*) $tU_0/\delta^*_{in} = 3350$; (*b*) $tU_0/\delta^*_{in} = 4415$.

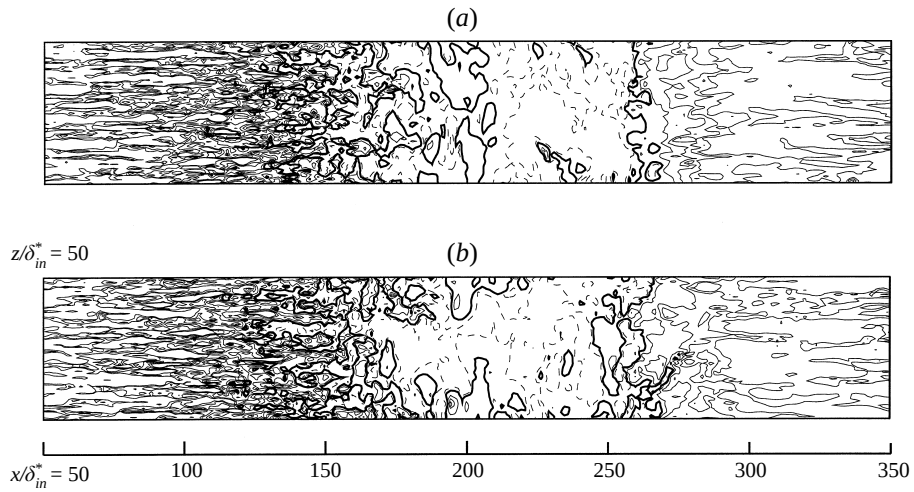

FIGURE 6. Instantaneous skin friction coefficient contours: ———, positive; – – – –, negative; thick solid lines correspond to $C_f = 0$. (*a*) $tU_0/\delta^*_{in} = 4415$; (*b*) $tU_0/\delta^*_{in} = 5053$.

Simpson (1991) made similar observations: he reported that λ_z increases by almost an order of magnitude after detachment. Since large-scale structures are formed in the detached shear layer as a result of the roll-up process and then propagate downstream, the boundaries of the detachment and reattachment regions fluctuate with time. It is clear that spanwise lines of detachment and reattachment do not move up- and downstream as a unit in figure 6. Their oscillatory behaviour can be illustrated by trajectories of the instantaneous motion of detachment and reattachment points in figures 7 and 8. These figures show the time history of the location of zero C_f of

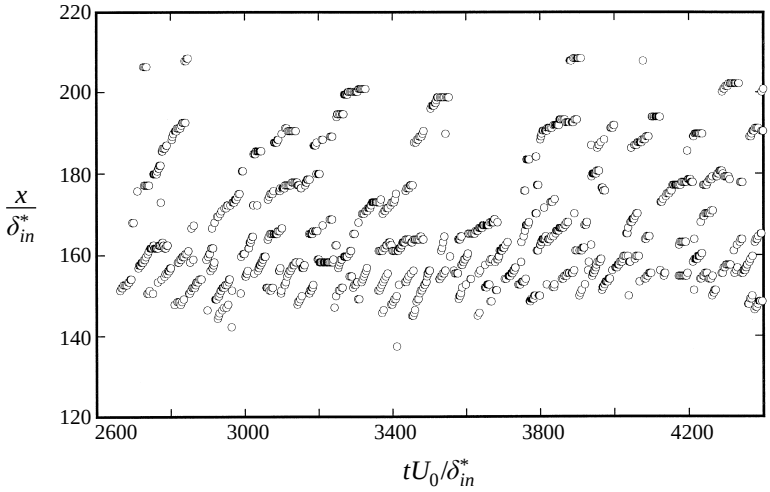

FIGURE 7. Locations of spanwise-averaged detachment point.

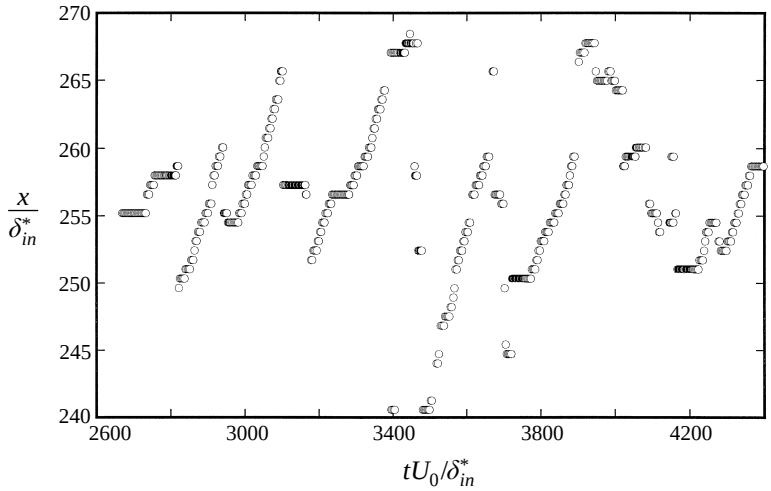

FIGURE 8. Locations of spanwise-averaged reattachment point.

the spanwise-averaged flow field. Figure 8 shows that the movement of the spanwise-averaged reattachment line is rather well defined compared to the detachment line (figure 7). The trajectories show the breathing pattern seen in the backward-facing step flow by Le *et al.* (1997). The linear growth was followed by a subsequent bursting of the recirculating zone in the backstep flow. The same interpretation can be given here in addition to the unsteady movement of the detachment zone in the streamwise direction.

3.3. *Instantaneous vorticity field*

Figure 9 shows contours of instantaneous spanwise vorticity in the (x, y)-plane at the mid-point of the domain. Turbulent structures from upstream of the separation bubble move upwards into the shear layer in the detachment region and then turn

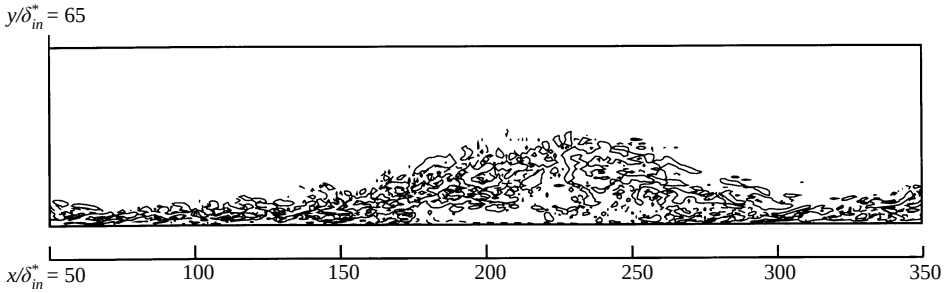

FIGURE 9. Instantaneous spanwise vorticity contours. ———, 0.047 U_0/δ^*_{in}; – – – –, –0.047 U_0/δ^*_{in}.

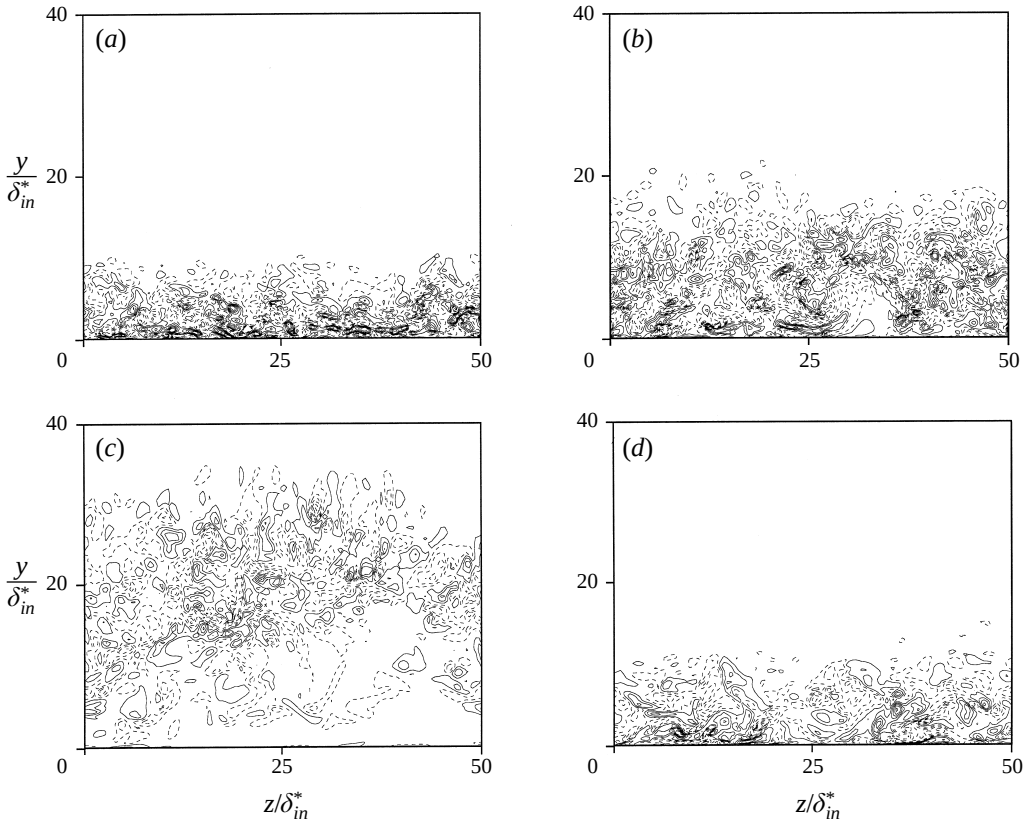

FIGURE 10. Contours of instantaneous streamwise vorticity: ———, positive; – – – –, negative. (*a*) $x/\delta^*_{in} = 120$; (*b*) $x/\delta^*_{in} = 160$; (*c*) $x/\delta^*_{in} = 220$; (*d*) $x/\delta^*_{in} = 320$. Contours: from –0.5 to 0.46 (U_0/δ^*_{in}) with increments of 0.08 (U_0/δ^*_{in}).

around the bubble, subsequently impinge on the wall in the reattachment region. After the reattachment, the shear layer changes to a boundary layer. However, as shown in figure 21, the relaxation from the characteristics of a typical shear layer to a boundary layer is a slow process. The flow in the detached shear layer appears to be qualitatively similar to a plane mixing layer.

Contours of streamwise vorticity in a (y, z)-plane are shown in figure 10. Far upstream of the separation bubble ($x/\delta^*_{in} = 120$), vortical structures are mainly

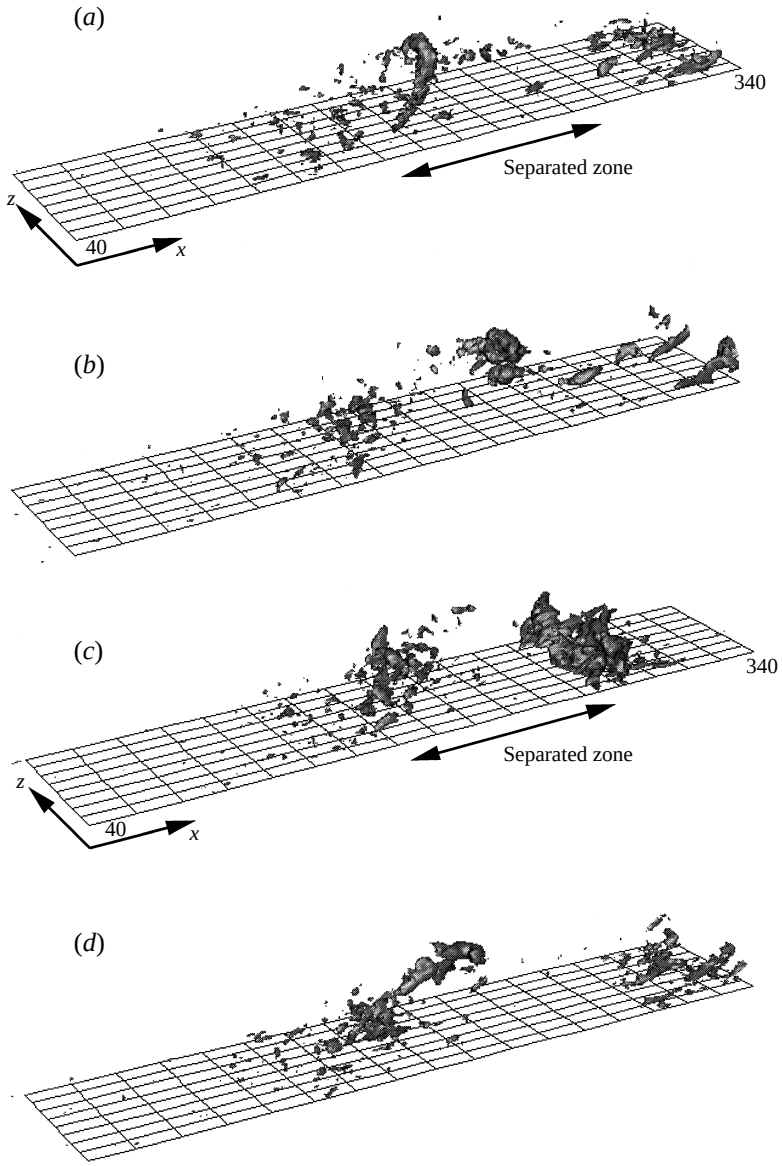

FIGURE 11. Iso-surfaces of instantaneous pressure fluctuations. Iso-value: $p'/\rho U_0^2 = -0.0185$. (*a*) $tU_0/\delta^*_{in} = 3238$; (*b*) $tU_0/\delta^*_{in} = 3350$; (*c*) $tU_0/\delta^*_{in} = 3463$; (*d*) $tU_0/\delta^*_{in} = 3575$.

confined to the inner region of the boundary layer. Moving downstream, vortices are lifted into the shear layer and a region of negligible vorticity appears near the wall in the detachment region ($x/\delta^*_{in} = 160$). In the middle of the separation bubble ($x/\delta^*_{in} = 220$), most of the vortices which arrive from the upstream boundary layer are weakened and lifted above the separation bubble. Then, they turn around the bubble and impinge on the wall in the reattachment region and convect downstream ($x/\delta^*_{in} = 320$). It appears that the separation bubble acts like a streamlined obstacle and the flow passes by the bubble smoothly without much penetration into the separation zone.

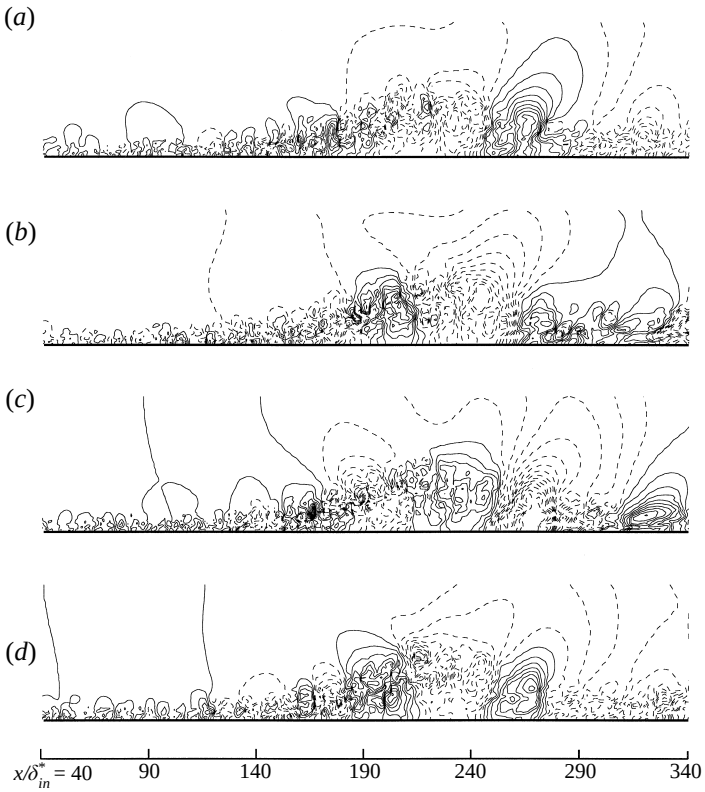

FIGURE 12. Contours of spanwise-averaged pressure fluctuations in an (x, y)-plane: ———, positive; – – – –, negative. (*a*) $tU_0/\delta^*_{in} = 3238$; (*b*) $tU_0/\delta^*_{in} = 3350$; (*c*) $tU_0/\delta^*_{in} = 3463$; (*d*) $tU_0/\delta^*_{in} = 3575$. Contours: $p'/\rho U_0^2$ are from -0.013 to 0.012 with increments of 0.0014.

3.4. *Instantaneous pressure field*

The formation of large-scale structures can be illustrated by examining the pressure field; low-pressure regions often correspond to the cores of vortical structures. Iso-surfaces of negative instantaneous pressure fluctuations are plotted at four different times in figure 11. At $t = 3238\delta^*_{in}/U_0$, an arch-like structure appears in the shear layer. At the later time $t = 3350\delta^*_{in}/U_0$, the tip of this structure is seen passing over the separated zone. Such structures grow very rapidly, agglomerate and then impinge on the wall ($t = 3463\delta^*_{in}/U_0$). As large-scale structures propagate downstream, they lose their coherence. However, the process is cyclical and new structures are found near the detachment zone, as in figure 11(*d*).

The fluctuation of the reattachment point shown in figure 8 can be related to the passage of large-scale structures of figure 11. As a large-scale structure grows in the shear layer ($t = 3238\delta^*_{in}/U_0$), the reattachment location travels downstream at approximately constant velocity, given by the slopes in figure 8. Later, the structure collapses and impinges on the wall ($t = 3463\delta^*_{in}/U_0$), causing a sudden drop of the reattachment location as the vestiges of the structure convect downstream. As another large-scale structure grows ($t = 3575\delta^*_{in}/U_0$), the reattachment point travels downstream again.

The characteristic frequency of these large structures can be roughly deduced from figure 8. The shedding process is not periodic and the characteristic time (time

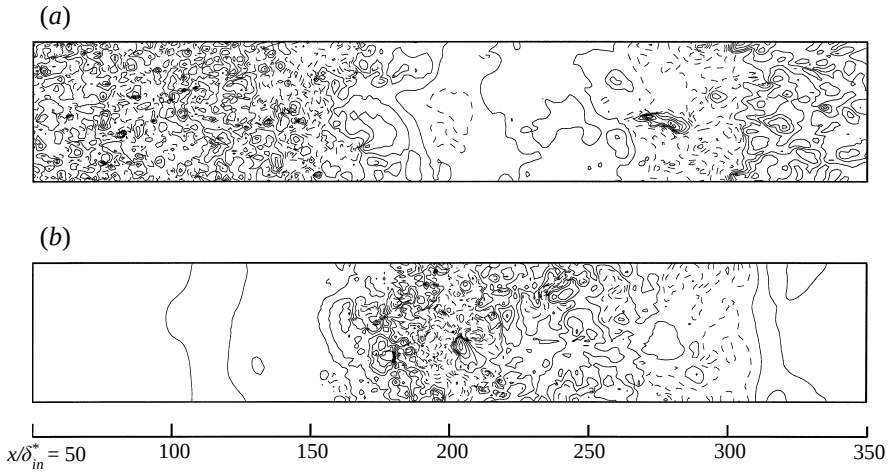

FIGURE 13. Contours of instantaneous pressure fluctuations in the (x, z)-plane: ———, positive; – – – –, negative. (*a*) $y/\delta^*_{in} = 0$; (*b*) $y/\delta^*_{in} = 15$.

interval between two peaks in figure 8) varies from $tU_0/\delta^*_{in} = 100$ to 400. Thus, the characteristic Strouhal number $St = f\delta^*_{in}/U_0$ of the most energetic structures ranges between 0.0025 and 0.01. In Le *et al.*'s (1997) study of backward-facing step flow, the Strouhal number corresponding to the dominant frequency is $St = f\delta^*_{in}/U_0 \approx 0.007$.

Figure 12 shows the spanwise-averaged pressure fluctuations in an (x, y)-plane at the same representative times considered in figure 11. The iso-surfaces shown in figure 11 roughly correspond to the dotted contours. This plot clearly shows the difference in eddy length scales between the far upstream and the separated zone. The small-scale structures grow rapidly in the shear layer and the resulting two-dimensional roller-type structures convect downstream. In the shear layer near the detachment region, an alternating flow pattern (positive and then negative contours of pressure fluctuations) develops. This is attributed to the passage of large vortices since the pressure is relatively low in the cores of vortices and it is relatively high between two cores.

Contours of instantaneous pressure fluctuations in two (x, z)-planes are shown in figure 13. As illustrated in figure 11, the wall-pressure fluctuations are reduced in the separated zone, and enhanced in the reattachment region. Away from the wall ($y/\delta^*_{in} = 15$), the pressure fluctuations have significantly increased above the separation bubble. This increase is thought to be due to the movement of structures which contribute to the generation of pressure fluctuation away from the wall. Turbulence stresses generated by the shear layer eddies may contribute significantly to the noise emanating from separated boundary layers.

3.5. *Flow reversal*

For steady free-stream separating turbulent boundary layers, the following set of definitions of the detachment and reattachment states near the wall has been proposed by Simpson (1981): *incipient detachment* (ID) occurs with instantaneous backflow 1% of the time ($\gamma_u = 0.99$) (here, γ_u is the fraction of time that the flow moves downstream); *intermittent transitory detachment* (ITD) occurs with instantaneous backflow 20% of the time ($\gamma_u = 0.80$); *transitory detachment* (TD) occurs with instantaneous backflow 50% of the time ($\gamma_u = 0.50$); and *detachment* (D) occurs where

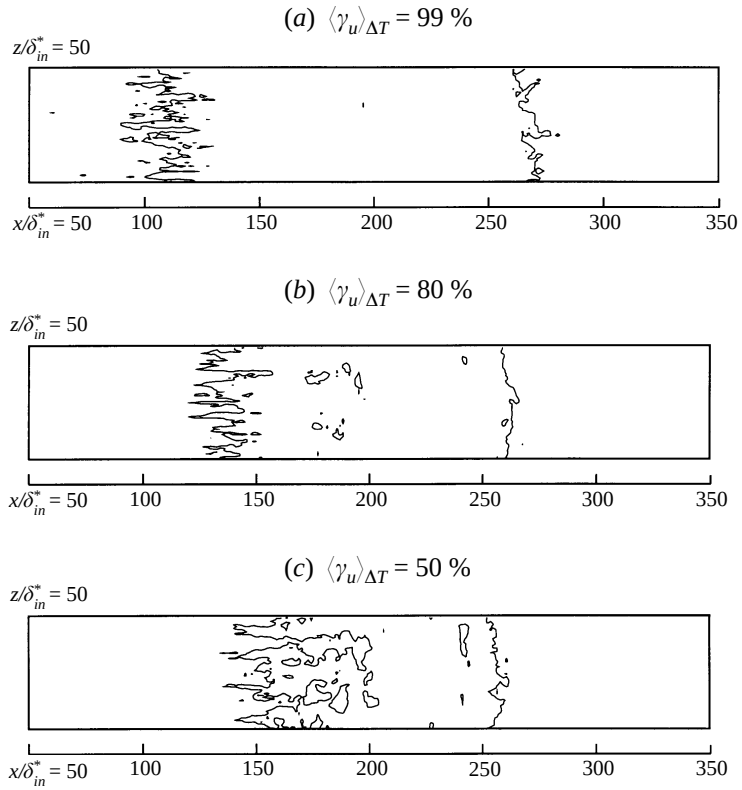

FIGURE 14. Contours of $\langle\gamma_u\rangle_{\Delta T}$ (fraction of time that the flow moves downstream for the time period of $300\delta^*_{in}/U_0$) in an (x,z)-plane very near the wall ($y/\delta^*_{in} = 0.0042$).

the time-averaged wall shearing stress is zero. Figure 14 shows three contours of $\langle\gamma_u\rangle_{\Delta T}(\langle\gamma_u\rangle_{\Delta T} = 0.99, 0.80, 0.50)$ in the (x,z)-plane at $y/\delta^*_{in} = 0.0042$. Here, $\langle\gamma_u\rangle_{\Delta T}$ was calculated over the time span of $300\delta^*_{in}/U_0$ with the purpose of illustrating the highly unsteady behaviour in the detachment zone. As discussed in § 3.2, a spanwise line of detachment does not move up- and downstream as a unit and is much more complicated than that of reattachment. Its irregular shape in the detachment region is related to the streak-like structures which arrive from upstream of the separation bubble. Inside the separated zone, there are several isolated zones of $\langle\gamma_u\rangle_{\Delta T} = 0.5$ which are attributed to the high-momentum fluid elements which penetrate into the separation bubble from regions away from the wall. This is the reason for having multiple locations of zero C_f at each instant seen in figure 7. Compared to detachment process, the reattachment region is relatively well-defined and does not show signatures of streak-like structures in figure 14. In figure 15, the spanwise-averaged fraction of time of forward flow ($\overline{\gamma}_u$) very near the wall is shown. $\overline{\gamma}_u$ does not decrease monotonically with x through the detachment region, whereas it increases more monotonically through the reattachment region. This oscillatory behaviour is partly due to the insufficient number of statistical samples (for this particularly sensitive quantity) but at the very least indicates the high intermittency in the detachment region. We expect that more samples (or equivalently, longer averaging time) would smooth the profile, but rather slowly for the same reason given for the budgets of turbulence intensities and mean momentum equations. In view of the shedding process of large-scale structures in

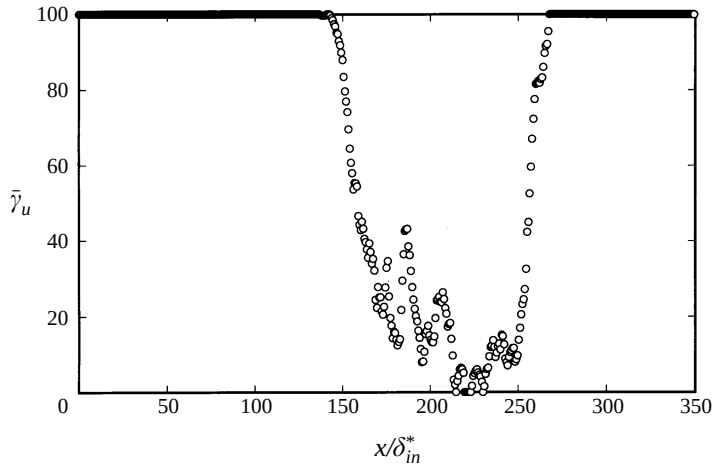

FIGURE 15. Spanwise-averaged fraction of time ($\bar{\gamma}_u$) that the flow moves downstream very near the wall ($y/\delta^*_{in} = 0.0042$).

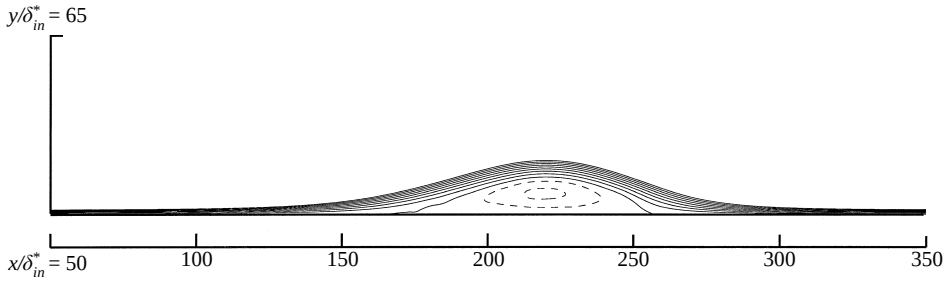

FIGURE 16. Mean streamlines.

§ 3.4, the total averaging time of the present work, $T_{ave} = 2250\delta^*_{in}/U_0$, is approximately equivalent to 7–9 passages of those structures (assuming the characteristic time of the structures is about (250–300) δ^*_{in}/U_0). There is a small region of $\bar{\gamma}_u = 0$, which indicates that the flow moves upstream all the time there. Patrick's (1987) experiment on a massively separated flow also shows the presence of regions of $\bar{\gamma}_u = 0$ inside the bubble. The locations corresponding to $\bar{\gamma}_u = 0.5$ are approximately $x/\delta^*_{in} = 157$ and 256 from figure 15.

3.6. *Detachment and reattachment lengths*

The mean streamlines are shown in figure 16. The height of the separation bubble is about $22\theta_{in}$ (or $13\delta^*_{in}$) and the length of the bubble is about $170\theta_{in}$ (or $99.5\delta^*_{in}$). The intersections of the mean dividing streamline ($\psi = 0$) with the wall are $x/\delta^*_{in} = 158$ and 257. The mean detachment and reattachment locations determined by the locations where $\bar{\gamma}_u = 0.5$ are $x/\delta^*_{in} = 157$ and 256 as shown in § 3.5. The mean skin friction and wall-pressure coefficients are shown in figure 17. The locations of zero wall-shear stress ($\bar{\tau}_w = 0$) are at $x/\delta^*_{in} = 158$ and 256. Thus, values determined by the three different definitions of detachment and reattachment are in good agreement. The location of the detachment has larger variation because this region is more complicated than reattachment as explained in the previous section. The wall-pressure coefficient shows that the flow develops under a ZPG near the inlet and then encounters increasingly

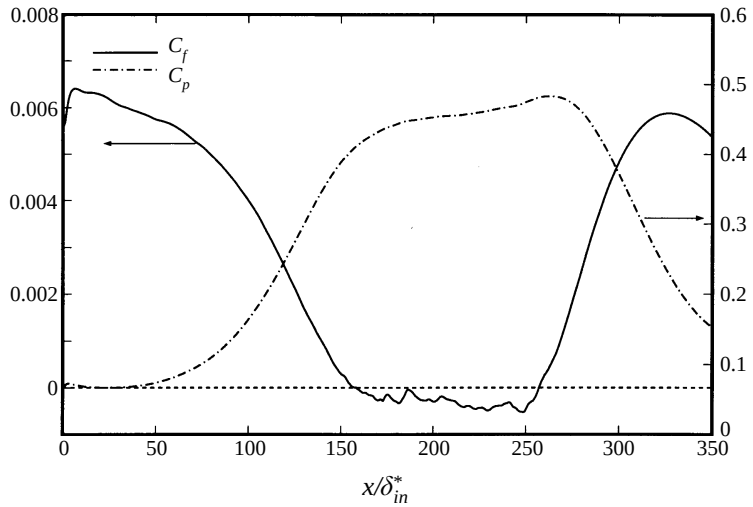

FIGURE 17. Skin-friction and mean wall-pressure coefficients based on U_0.

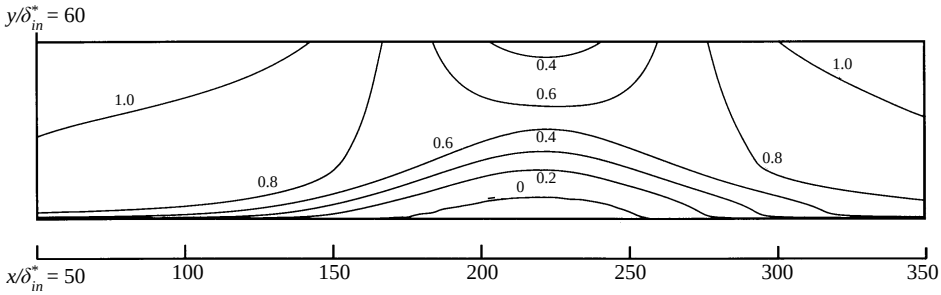

FIGURE 18. Contours of mean streamwise velocity.

positive pressure gradient up to the detachment region. The flattened top of the pressure distribution is due to the blockage by the abruptly thickened boundary layer, which displaces the outer layer flow and thus relieves the pressure peak. This is a frequently observed characteristic of separated bubbles. Mean detachment occurs where the mean pressure gradient starts to decrease.

3.7. *Mean velocity*

Contours of mean streamwise and wall-normal velocities are shown in figures 18 and 19. Mean streamwise velocity decelerates significantly in the free stream, producing the large streamwise APG. The wall-normal velocity is positive up to the middle of the separation bubble and the contours of positive and negative wall-normal velocities have very similar half-circular shapes. In the middle of the separation bubble ($x/\delta^*_{in} = 220$), the streamwise velocity remains negative up to $y/\delta^*_{in} = 7.0$ or about half of the separation bubble height. The magnitude of the maximum negative velocity at this location is about $0.06U_0$. The magnitude of velocity fluctuations in the backflow region are comparable to or higher than the mean backflow and the time-averaged mean flow is not a good approximation to the unsteady, instantaneous flow behaviour. In the recovery region ($x/\delta^*_{in} = 300, 320$), streamwise velocity profiles

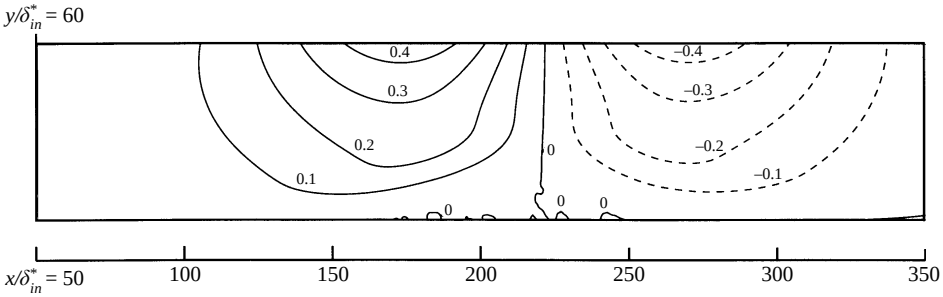

FIGURE 19. Contours of mean wall-normal velocity: ——— positive; – – – – negative.

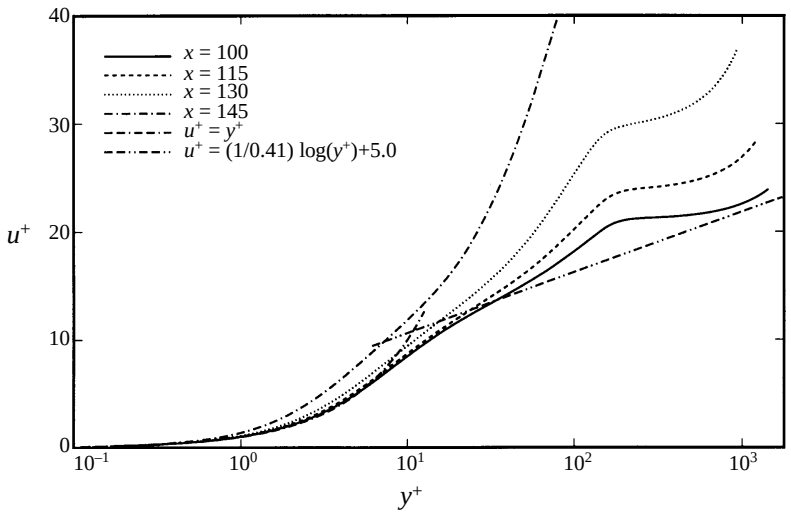

FIGURE 20. Mean streamwise velocity profiles in wall coordinates before detachment.

show an inflection point near the wall indicating that the flow is still in the process of recovering.

Figure 20 shows the streamwise velocity profiles in wall coordinates upstream of detachment. Moving downstream, the velocity profiles deviate significantly from the standard log–law. Simpson (1989) observed that the mean flow upstream of separation obeys the law of the wall as long as the ratio of local maximum Reynolds shear stress to local wall shear stress is less than 1.5. This ratio varies from 1.3 (at $x/\delta^*_{in} = 100$) to 9.8 (at $x/\delta^*_{in} = 145$) in figure 20 and the 'law of the wall' does not hold at any streamwise locations. Since the Reynolds number of the present flow is low compared to that of Simpson's experiment, the log layer of the velocity profile is not very well-developed as shown in Spalart (1988) and deviates from the law of the wall earlier than in the experiment.

In figure 21, the progression of the velocity profiles in the recovery region is shown. A similar behaviour can be seen in the recovery region in Chandrsuda & Bradshaw (1981), Patrick (1987), Le *et al.* (1997). Flow is re-developing under very mild APG in Chandrsuda & Bradshaw and Le *et al.*'s studies, whereas it is recovering in strong FPG in Patrick's and the present studies. As discussed by Chandrsuda & Bradshaw, the persistence of the dip below the log-law implies the persistence of abnormally

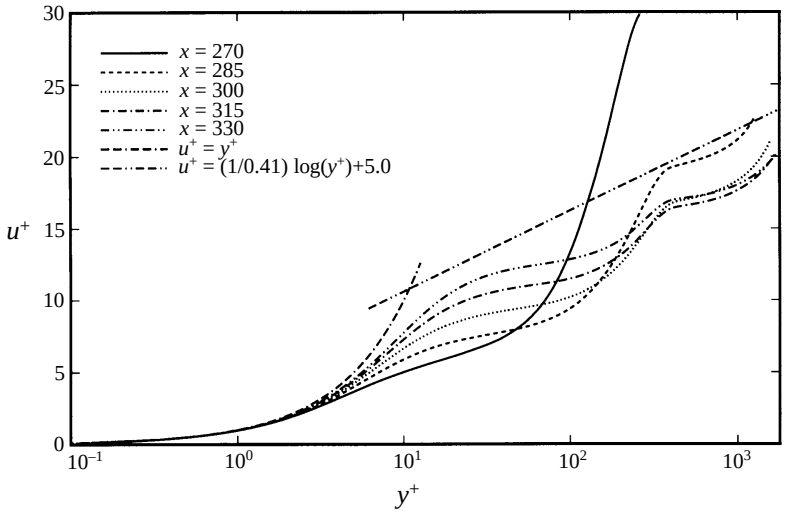

FIGURE 21. Mean streamwise velocity profiles in wall coordinates after reattachment.

large length scales which indicates that large energetic eddies formed in the shear layer survive a long time before breaking up into smaller dissipative eddies.

3.8. *Turbulence intensities and Reynolds shear stress*

Contours of r.m.s. profiles of turbulence intensities and the Reynolds shear stress are displayed in figure 22(*a–d*). All r.m.s. values are normalized by the inlet free-stream velocity.

The maximum $(\overline{u'^2})^{1/2}$ occurs in the shear layer above the detachment region. It is significantly reduced inside the separation bubble. Since the turbulent structures are lifted and turn around the bubble, it can be inferred that the locus of large $(\overline{u'^2})^{1/2}$ is in the middle of the shear layer developing around the separation bubble. In the recovery region, the familiar near-wall peak of $(\overline{u'^2})^{1/2}$ develops as the flow is recovering. $(\overline{v'^2})^{1/2}$ and $(\overline{w'^2})^{1/2}$ show similar behaviour. At $x/\delta^*_{in} = 220$, velocity fluctuations in the backflow region are comparable to the mean backflow. In the reattachment region ($x/\delta^*_{in} = 270$), the magnitudes of three components of turbulent intensities are approximately the same and in the recovery region ($x/\delta^*_{in} = 320$), the near-wall peaks reappear indicating the boundary layer is re-developing.

In the case of Reynolds shear stress, the maximum occurs downstream of reattachment. Local Reynolds shear stress maxima are significantly reduced up to the middle of the separation bubble. It increases thereafter and reaches its maximum value downstream of the reattachment region. This behaviour is somewhat different from that in the backward-facing step flow of Le *et al.* (1997): in their study, the maximum Reynolds shear stress decreases after the reattachment, but this drop is delayed in the present study. In their study of separated flow on a smooth, axisymmetric body, Alving & Fernholz (1996) reported the same behaviour of maximum Reynolds shear stress as in the present study. This is thought to be an important difference between the backward-facing step flows and flows with separation due to APG. As in attached flows, the loci of the maximum Reynolds shear stress as well as other Reynolds stress components occur in the region where $\partial U/\partial y$ takes its maximum value, which develops around the separation bubble.

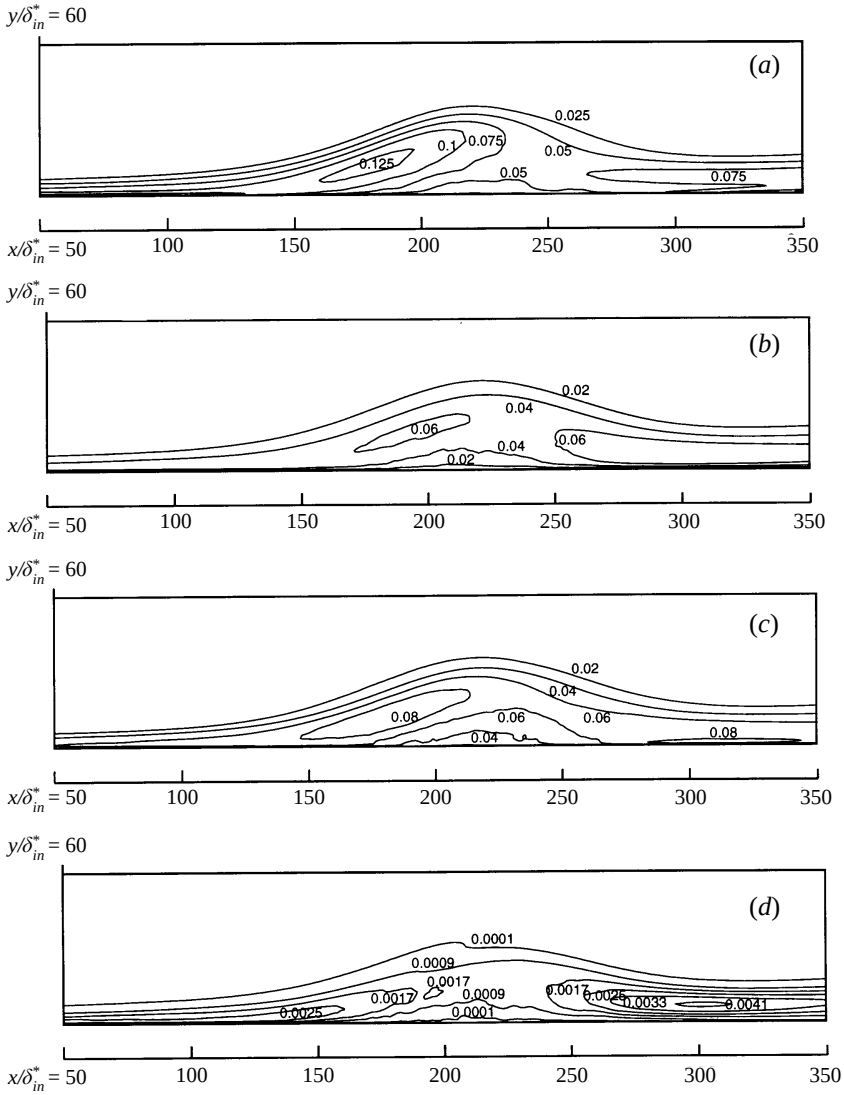

FIGURE 22. Contours of turbulence intensities: (*a*) longitudinal component $(\overline{u'^2})^{1/2}/U_0$); (*b*) wall-normal component $(\overline{v'^2})^{1/2}/U_0$); (*c*) spanwise component $(\overline{w'^2})^{1/2}/U_0$); (*d*) Reynolds shear stress $(-\overline{u'v'}/U_0^2)$.

3.9. *Kinetic energy budget*

The budgets for the turbulent kinetic energy are shown in figures 23–26. Far upstream of the separation bubble (not shown here), the budgets are similar to those of typical APG turbulent boundary layer. At $x/\delta^*_{in} = 160$ (in the detachment region), the budget is very similar to that of a plane mixing layer (Rogers & Moser 1993). Both production and dissipation have maxima at the same location in the shear layer and the ratio of them is about 64%. The velocity–pressure-gradient term is negligible in most of the layer except very near the wall where dissipation and viscous diffusion terms are important. The turbulent transport term removes energy from the shear layer and delivers it to the near-wall region.

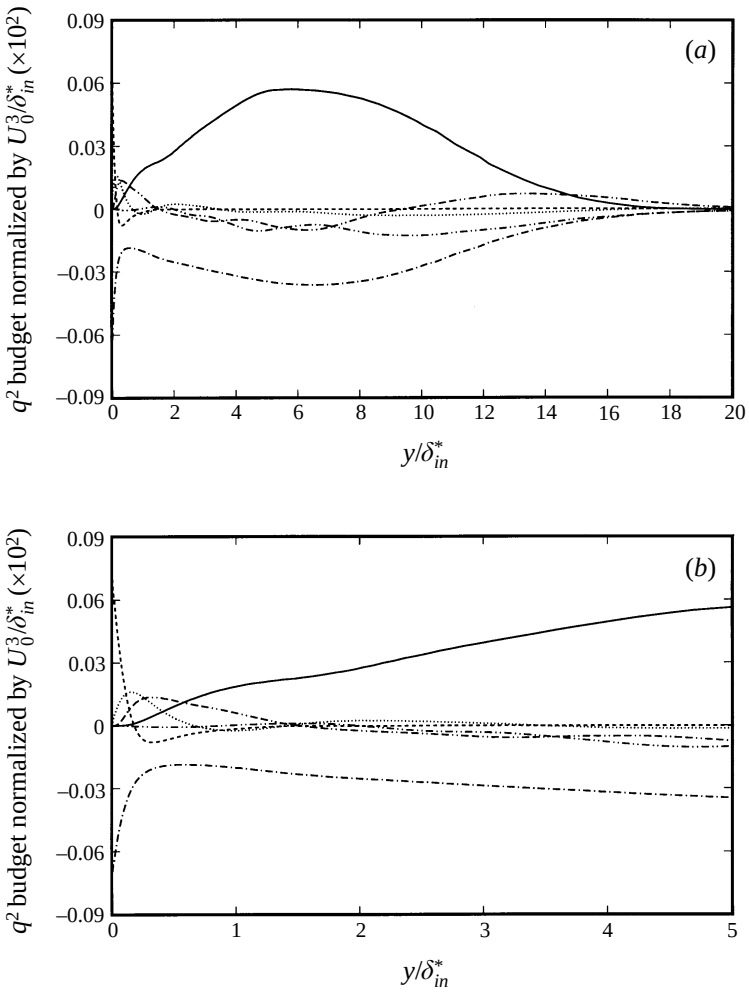

FIGURE 23. Turbulent kinetic energy budget at $x/\delta_{in}^* = 160$: ———, production; —·—, dissipation; – – – –, viscous diffusion; —··—, convection; — — ··, turbulent transport; ·····, velocity pressure gradient. (*a*) Away from the wall; (*b*) near the wall.

In the middle of the separation bubble ($x/\delta_{in}^* = 220$), the dissipation term is a main consuming term throughout the layer and the production and convection terms are dominant producing terms in the shear layer. Negligible turbulence energy production occurs in the mean backflow region. The main contribution to the convection term is from the longitudinal component (C_{11}). C_{11} consists of two terms:

$$C_{11} = -U\frac{\partial \overline{u'u'}}{\partial x} - V\frac{\partial \overline{u'u'}}{\partial y}.$$

Inside the separation bubble, the first term is dominant because both U and $\partial\overline{u'u'}/\partial x$ are greater than V and $\partial\overline{u'u'}/\partial y$, respectively as shown in figures 18–22. Very near the wall, the dissipation is in balance with the viscous diffusion as in a viscous sublayer of attached boundary layers.

Through the reattachment and subsequent recovery region, the magnitudes of most

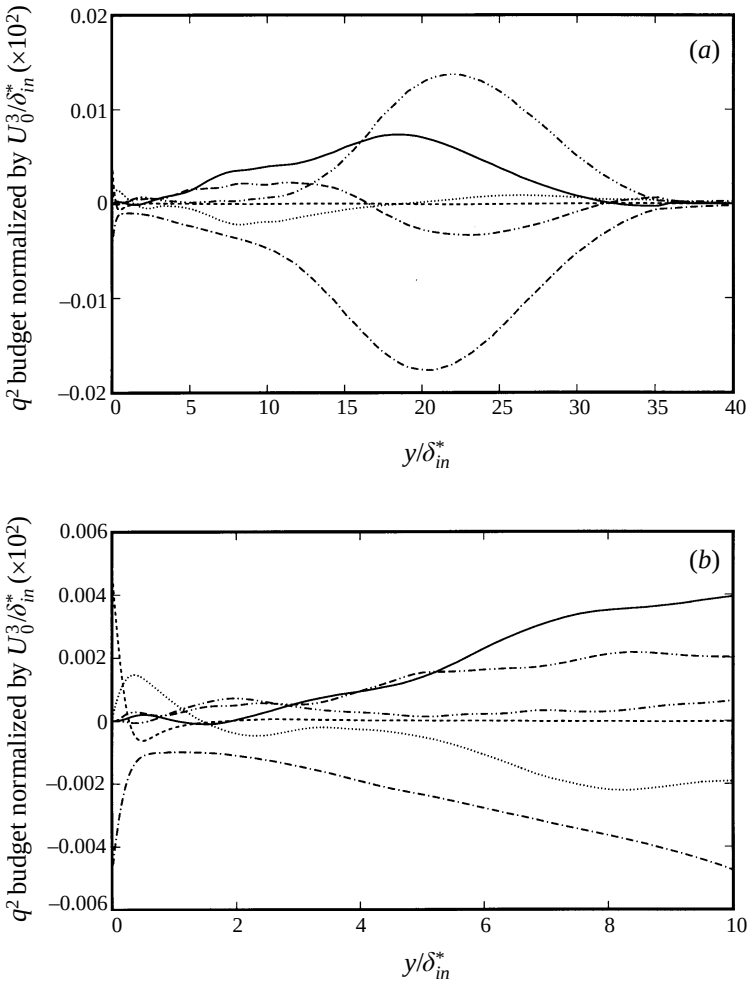

FIGURE 24. As figure 23 but at $x/\delta_{in}^* = 220$.

of the terms increase with x. In the reattachment region ($x/\delta_{in}^* = 270$), the budget is qualitatively similar to that of backward-facing step flow (Le *et al.* 1997). The production term is a dominant producing term in the outer layer, and dissipation, viscous diffusion and velocity–pressure-gradient terms are important very near the wall. At $x/\delta_{in}^* = 320$, the profiles very near the wall show that the flow is recovering to a turbulent boundary layer. However, in the outer layer, the influence of the shear layer is still present.

4. Conclusion

Direct numerical simulation of a separated turbulent boundary layer over a flat plate was performed. The flow separates due to the large adverse pressure gradient induced by a suction–blowing velocity distribution along the upper boundary. Neither instantaneous detachment nor reattachment points are fixed in space but fluctuate significantly upstream and downstream. This oscillatory behaviour was illustrated by the trajectories of the location of the zero C_f of spanwise-averaged flow field. The

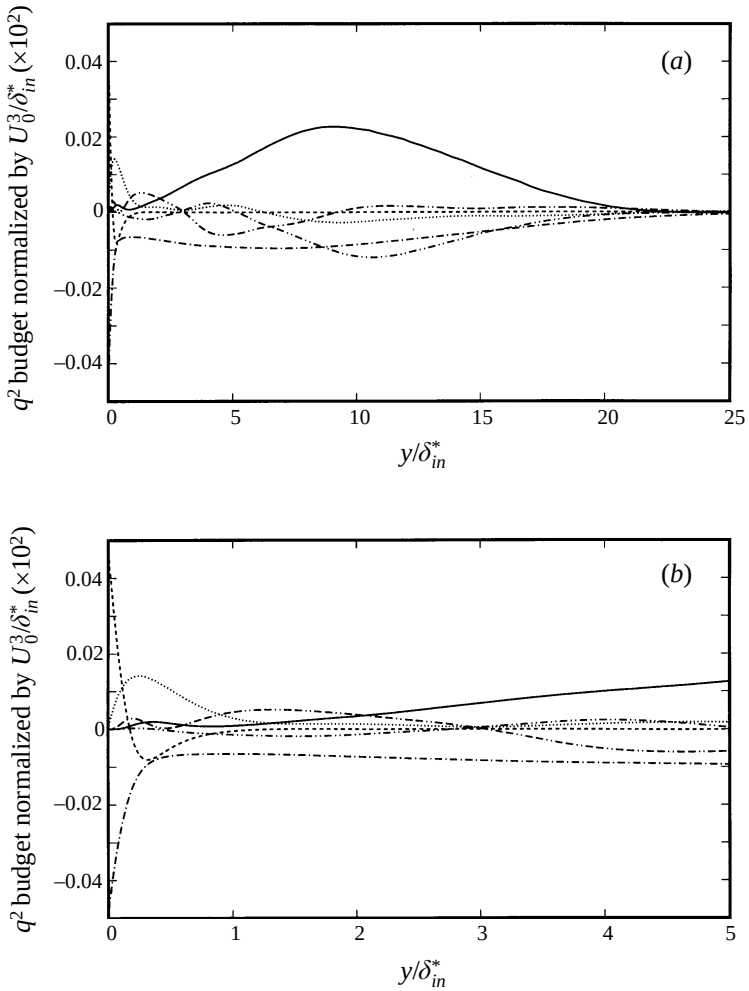

FIGURE 25. As figure 23 but at $x/\delta_{in}^* = 270$.

detachment point is not clearly defined and the detachment process occurs over a region instead of a point. However, the movement of the spanwise-averaged line of reattachment is rather well defined. The mean detachment and reattachment locations determined by the three different definitions, i.e. (i) location of 50% forward flow fraction, (ii) mean dividing streamline ($\psi = 0$), (iii) location of zero wall-shear stress ($\overline{\tau}_w = 0$), result in virtually identical values.

Instantaneous vorticity contours show that turbulent structures emanating upstream of the separation bubble move away from the wall into the shear layer in the detachment region and then turn around the bubble. Subsequently, they impinge on the wall in the reattachment region. The flow in this shear layer is qualitatively similar to a plane mixing layer. The locations of the maximum turbulence intensities as well as Reynolds stress occur in the middle of the shear layer. In the detached flow region, Reynolds shear stresses and their gradients are large away from the wall and thus the largest pressure fluctuations are in the middle of the shear layer. However, pressure fluctuations inside the separation bubble are suppressed.

Iso-surfaces of the negative pressure fluctuations which correspond to the core

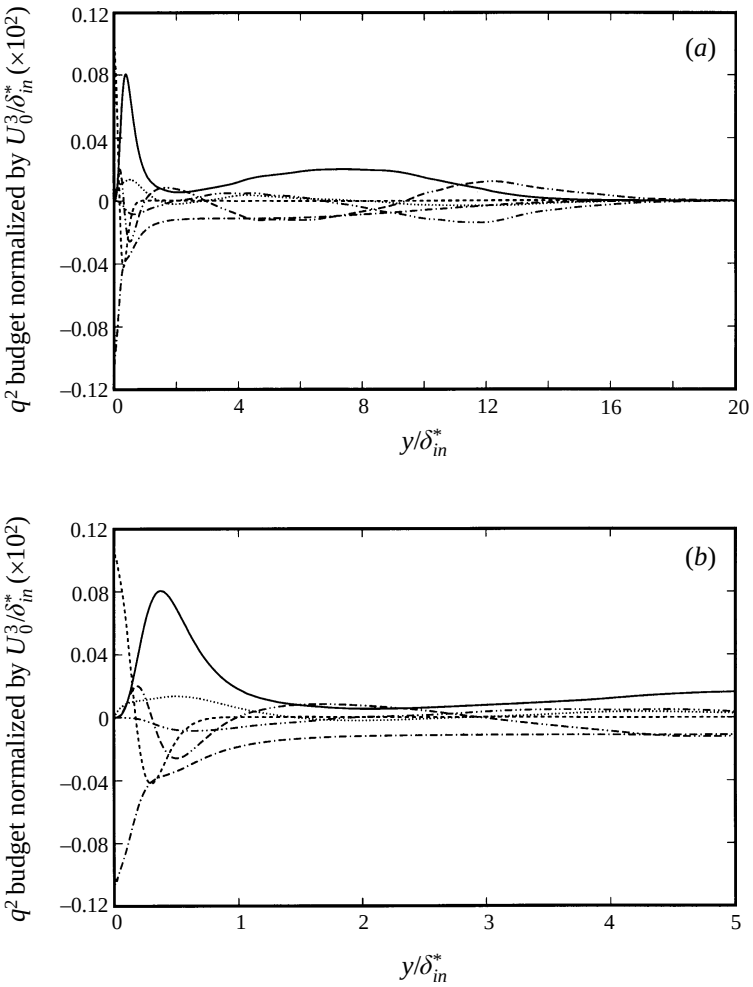

FIGURE 26. As figure 23 but at $x/\delta_{in}^* = 320$.

region of the vortices show that large-scale structures grow in the shear layer and agglomerate. They then impinge on the wall and subsequently convect downstream. The characteristic Strouhal number $St = f\delta_{in}^*/U_0$ ranges between 0.0025 and 0.01.

The kinetic energy budget in the detachment region is very similar to that of a plane mixing layer. Both production and dissipation have maxima at the same location in the shear layer and the ratio of them is about 0.64. In the kinetic energy budget inside the separation bubble, the dissipation term is a main consuming term throughout the layer and the production and convection terms are dominant producing terms. Through the reattachment and subsequent recovery region, the magnitudes of most terms increase with x, and the influence of the shear layer is present well beyond the reattachment point.

This work was supported by the Office of Naval Research. The authors gratefully acknowledge Dr Meng Wang for his helpful comments and suggestions on a draft of this paper.

REFERENCES

Adams, E. W. & Eaton, J. K. 1988 An LDV study of the backward-facing step flow including the effects of velocity bias. *Trans. ASME J. Fluids Engng* **110**, 275–282.

Alving, A. E. & Fernholz, H. H. 1996 Turbulence measurements around a mild separation bubble and downstream of reattachment. *J. Fluid Mech.* **322**, 297–328.

Briley, W. R. & McDonald, H. 1975 Numerical prediction of incompressible separation bubbles. *J. Fluid Mech.* **69**, 631–656.

Chandrusuda, C. & Bradshaw, P. 1981 Turbulent structure of a reattaching mixing layer. *J. Fluid Mech.* **110**, 171–194.

Coleman, G. N. & Spalart, P. R. 1993 Direct numerical simulation of a small separation bubble. In *Near-Wall Turbulence Flows* (ed. C. G. Speziale & B. E. Launder), pp. 277–286. Elsevier.

Cutler, A. D. & Johnston, J. P. 1984 Adverse pressure gradient and separating turbulent boundary layer flows: The effect of disequilibrium in initial conditions. *Rep.* MD-46. Thermosciences Div., Mech. Engng Dept., Stanford University.

Harlow, F. H. & Welch, J. E. 1965 Numerical calculation of time dependent viscous incompressible flow of fluid with free surface. *Phys. Fluids* **8**, 2182–2189.

Kline, S. J., Cantwell, B. J. & Lilley, G. M. 1982 *AFOSR-HTTM-Stanford Conference on Complex Turbulent Flows: Comparison of Computation and Experiment*, 2.

Le, H. & Moin, P. 1991 An improvement of fractional step methods for the incompressible Navier–Stokes equations. *J. Comput. Phys.* **92**, 369–379.

Le, H., Moin, P. & Kim, J. 1997 Direct numerical simulation of turbulent flow over a backward facing step. *J. Fluid Mech.* **330**, 349–374.

Lee, S., Lele, S. K. & Moin, P. 1992 Simulation of spatially evolving turbulence and the applicability of Taylor's hypothesis in compressible flow. *Phys. Fluids* A **4**, 1521–1530.

Lowery, P. S. & Reynolds, W. C. 1986 Numerical simulation of a spatially-developing, forced plane mixing layer. *Rep.* TF-26. Thermosciences Div., Dept. of Mech. Engng, Stanford University.

Mahesh, K., Moin, P. & Lele, S. K. 1996 The interaction of a shock wave with a turbulent shear flow. *Rep.* TF-69. Thermosciences Div., Dept. of Mech. Engng, Stanford University.

Na, Y. & Moin, P. 1996 Direct numerical simulation of turbulent boundary layer with adverse pressure gradient and separation. *Rep.* TF-68. Thermosciences Div., Dept. of Mech. Engng, Stanford University.

Patrick, W. P. 1987 Flow filed measurements in a separated and reattached flat plate turbulent boundary layer. *NASA Contractor Rep.* 4052.

Pauley, L. L., Moin, P. & Reynolds, W. C. 1990 The structure of two-dimensional separation. *J. Fluid Mech.* **220**, 397–411.

Perry, A. E. & Fairlie, B. D. 1975 A study of turbulent boundary-layer separation and reattachment. *J. Fluid Mech.* **69**, 657–672.

Press, W. H., Flannery, B. P., Teukolsky, S. A. & Vetterling, W. T. 1992 *Numerical Recipes in Fortran*, 2nd. edn, pp. 644–649. Cambridge University Press.

Rogers, M. & Moser, R. 1993 Direct numerical simulation of a self similar turbulent mixing layer. *Phys. Fluids* A **6**, 903–923.

Shiloh, K., Shivaprasad, B. G. & Simpson, R. L. 1981 The structure of a separating turbulent boundary layer. Part 3. Transverse velocity measurements. *J. Fluid Mech.* **113**, 75–90.

Simpson, R. L. 1981 A review of some phenomena in turbulent flow separation in turbulent flow separation. *Trans. ASME: J. Fluids Engng* **103**, 520–533.

Simpson, R. L. 1985 Two-dimensional turbulent separated flow *AGARDograph* 287, vol. 1.

Simpson, R. L. Turbulent boundary layer separation. *Ann. Rev. Fluid Mech.* **21**, 205–234.

Simpson, R. L. 1991 The structure of the near-wall region of two-dimensional turbulent separated flow. *Phil. Trans. R. Soc. Lond.* A **336**, 5–17.

Simpson, R. L., Chew, Y. T. & Shivaprasad, B. G. 1981*a* The structure of a separating turbulent boundary layer. Part 1. Mean flow and Reynolds stresses. *J. Fluid Mech.* **113**, 23–51.

Simpson, R. L., Chew, Y. T. & Shivaprasad, B. G. 1981*b* The structure of a separating turbulent boundary layer. Part 2. Higher-order turbulence results. *J. Fluid Mech.* **113**, 53–73.

Simpson, R. L., Strickland, J. H. & Barr, P. W. 1977 Features of a separating turbulent boundary layer in the vicinity of separation. *J. Fluid Mech.* **79**, 553–594.

SPALART, P. R. 1988 Direct numerical simulation of a turbulent boundary layer up to $Re_\theta = 1410$. *J. Fluid Mech.* **187**, 61–98.

SPALART, P. R., MOSER, R. D. & ROGERS 1991 Spectral methods for the Navier–Stokes equations with one infinite and two periodic directions. *J. Comput. Phys.* **96**, 297–324.

WATMUFF, J. H. An experimental investigation of a low Reynolds number turbulent boundary layer subject to an adverse pressure gradient. *Ann. Res. Briefs, Center for Turbulence Research, NASA Ames Research Center/Stanford University*, pp. 37–49.